

**This is a self-archived version of an original article. This version may differ from the original in pagination and typographic details.**

**Author(s):** Nies, L.; Atanasov, D.; Athanasakis-Kaklamanakis, M.; Au, M.; Bernerd, C.; Blaum, K.; Chrysalidis, K.; Fischer, P.; Heinke, R.; Klink, C.; Lange, D.; Lunney, D.; Manea, V.; Marsh B., A.; Müller, M.; Mougeot, M.; Naimi, S.; Schweiger Ch.; Schweikhard, L.; Wienholtz, F.

**Title:** Refining the nuclear mass surface with the mass of  $^{103}\text{Sn}$

**Year:** 2025

**Version:** Published version

**Copyright:** © Authors

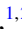
















**Rights:** CC BY 4.0

**Rights url:** <https://creativecommons.org/licenses/by/4.0/>

**Please cite the original version:**

Nies, L., Atanasov, D., Athanasakis-Kaklamanakis, M., Au, M., Bernerd, C., Blaum, K., Chrysalidis, K., Fischer, P., Heinke, R., Klink, C., Lange, D., Lunney, D., Manea, V., Marsh B., A., Müller, M., Mougeot, M., Naimi, S., Schweiger Ch., Schweikhard, L., Wienholtz, F. (2025). Refining the nuclear mass surface with the mass of  $^{103}\text{Sn}$ . *Physical Review C*, 111, Article 014315.  
<https://doi.org/10.1103/physrevc.111.014315>

Refining the nuclear mass surface with the mass of  $^{103}\text{Sn}$ 

L. Nies <sup>1,2,\*</sup> D. Atanasov <sup>3,†</sup> M. Athanasakis-Kaklamanakis <sup>1,4,‡</sup> M. Au <sup>1,5</sup> C. Bernerd,<sup>1</sup> K. Blaum <sup>6</sup>  
 K. Chrysalidis <sup>1</sup> P. Fischer <sup>2</sup> R. Heinke <sup>1</sup> C. Klink <sup>1,7</sup> D. Lange <sup>6</sup> D. Lunney <sup>8</sup> V. Manea <sup>8</sup> B. A. Marsh,<sup>1,§</sup>  
 M. Müller,<sup>6</sup> M. Mougeot <sup>9,6</sup> S. Naimi <sup>8</sup> Ch. Schweiger <sup>6</sup> L. Schweikhard <sup>2</sup> and F. Wienholtz <sup>7</sup>

<sup>1</sup>European Organization for Nuclear Research (CERN), 1211 Geneva 23, Switzerland

<sup>2</sup>Institut für Physik, Universität Greifswald, 17487 Greifswald, Germany

<sup>3</sup>LP2i Bordeaux, UMR5797, Université de Bordeaux, CNRS, F-33170 Gradignan, France

<sup>4</sup>KU Leuven, Instituut voor Kern- en Stralingsfysica, B-3001 Leuven, Belgium

<sup>5</sup>Johannes Gutenberg-Universität Mainz, 55099 Mainz, Germany

<sup>6</sup>Max-Planck-Institut für Kernphysik, 69117 Heidelberg, Germany

<sup>7</sup>Institut für Kernphysik, Technische Universität Darmstadt, 64289 Darmstadt, Germany

<sup>8</sup>Université Paris-Saclay, CNRS/IN2P3, IJCLab, 91405 Orsay, France

<sup>9</sup>Department of Physics, Accelerator laboratory, University of Jyväskylä, P.O. Box 35(YFL), FI-40014 University of Jyväskylä, Finland



(Received 23 October 2024; accepted 13 December 2024; published 9 January 2025)

Mass measurements with the ISOLTRAP mass spectrometer at CERN-ISOLDE improve mass uncertainties of neutron-deficient tin isotopes towards doubly magic  $^{100}\text{Sn}$ . The mass uncertainty of  $^{103}\text{Sn}$  was reduced by a factor of 4, and the new value for the mass excess of  $-67104(18)\text{keV}$  is compared with nuclear *ab initio* and density functional theory calculations. Based on these results and local trends in the mass surface, the masses of  $^{101,103}\text{Sn}$ , as determined through their  $Q_{\text{EC}}$  values, were found to be inconsistent with the new results. From our measurement for  $^{103}\text{Sn}$ , we extrapolate the mass excess of  $^{101}\text{Sn}$  to  $-60005(300)\text{keV}$ , which is significantly more bound than previously suggested. By correcting the mass values for  $^{101,103}\text{Sn}$ , we also adjust the values of  $^{104}\text{Sb}$ ,  $^{105,107}\text{Te}$ ,  $^{108}\text{I}$ ,  $^{109,111}\text{Xe}$ , and  $^{112}\text{Cs}$  near the proton drip line which are connected through their  $\alpha$  and proton  $Q$  values. The results show an overall smoothening of the mass surface, suggesting the absence of deformation energy above the  $N = 50$  shell closure.

DOI: [10.1103/PhysRevC.111.014315](https://doi.org/10.1103/PhysRevC.111.014315)

## I. INTRODUCTION

The heaviest self-conjugate ( $N = Z$ ) nucleus bound against proton emission,  $^{100}\text{Sn}$ , is one of the most interesting isotopes for nuclear research [1]. Its experimental investigation is important for testing our understanding of nuclear forces, especially since it is theorized to be a doubly magic nucleus with  $N = Z = 50$  nucleons. First experimentally observed in the 1990s at GANIL, France [2], and at GSI, Germany [3], it has the smallest  $\log(ft)$  value of any superallowed Gamow-Teller  $\beta$ -decaying nuclei [4], and it marks the endpoint of a

secluded island of  $\alpha$  emitters [5,6] and of the astrophysical  $r$  $p$  process [7–9].

Due to its small production cross section through nuclear reactions [10], experimental knowledge on  $^{100}\text{Sn}$  and its direct neighbors is, however, still sparse. Many investigations in this neutron-deficient area of the nuclear chart have been performed at facilities such as GSI, Germany, and RIKEN, Japan, using heavy primary beams such as  $^{112}\text{In}$  or  $^{124}\text{Xe}$  to produce rare isotopes through fragmentation processes [4,11–14] or fusion-evaporation reactions using the ion guide isotope separation online (IGISOL) technique [15,16] in Jyväskylä, Finland. Using the isotope separator online (ISOL) technique with 1.4 GeV protons accelerated onto a thick target at CERN-ISOLDE in Switzerland [17], masses of indium isotopes ( $Z = 49$ ) and their long-lived excited states were measured, including  $^{99}\text{In}$ , one proton below  $^{100}\text{Sn}$  [18,19], while laser spectroscopy has been performed on tin isotopes down to  $^{104}\text{Sn}$  [20] and Coulomb excitation down to  $^{106}\text{Sn}$  [21].

High-precision Penning-trap mass measurements on neutron-deficient tin isotopes were performed at the IGISOL mass separator and GSI, reaching down to  $^{104}\text{Sn}$  [8,22]. More recently, the CSRe storage ring in Lanzhou, China, allowed the direct measurement of  $^{103}\text{Sn}$  for the first time [23], followed by a Penning-trap measurement at the Facility for Rare Isotope Beams (FRIB), USA [24], and the TITAN

\*Contact author: [Lukas.Nies@cern.ch](mailto:Lukas.Nies@cern.ch)

<sup>†</sup>Present address: Belgian Nuclear Research Centre SCK CEN, Boeretang 200, 2400 Mol, Belgium.

<sup>‡</sup>Present address: Centre for Cold Matter, Imperial College London, London SW7 2AZ, United Kingdom.

<sup>§</sup>Deceased.

Published by the American Physical Society under the terms of the [Creative Commons Attribution 4.0 International](https://creativecommons.org/licenses/by/4.0/) license. Further distribution of this work must maintain attribution to the author(s) and the published article's title, journal citation, and DOI. Open access publication funded by CERN.

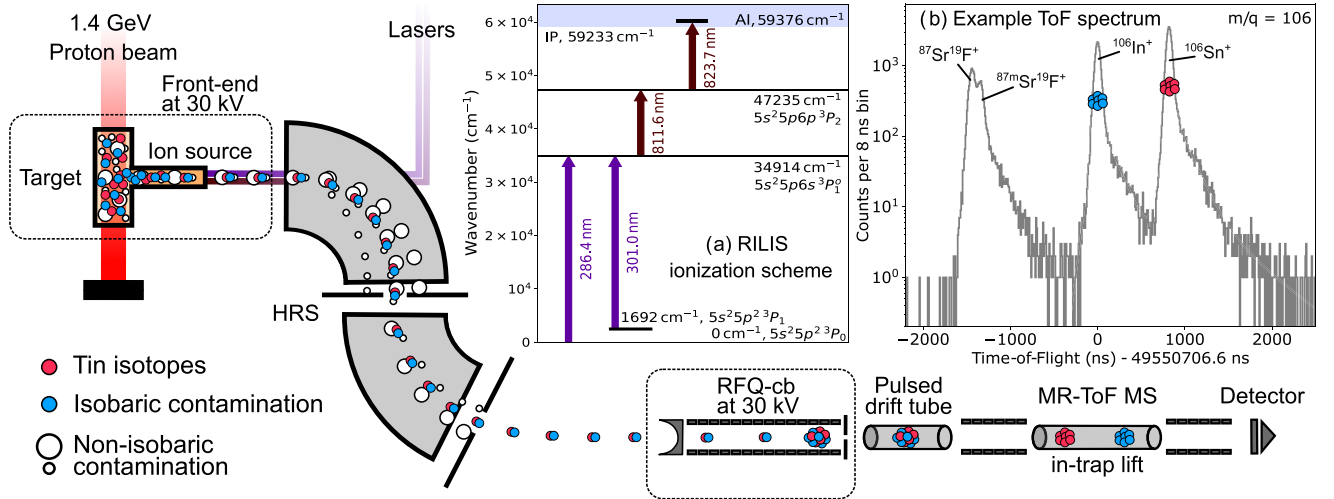


FIG. 1. Schematic of the apparatus. Protons with 1.4 GeV produce radioisotopes through nuclear reactions in the target material, where tin isotopes are vaporized and then laser ionized through resonance laser ionization [laser scheme in (a)]. Here, IP stands for the ionization potential of tin, and AI denotes the energy for autoionizing states. Tin isotopes (red circles) and parasitically ionized contamination (blue and white circles) are extracted at 30 keV and subsequently mass separated using two electromagnets (high-resolution separator, HRS). Ions with the selected mass-over-charge ratio  $m/q$  are collected in an ion cooler and buncher (RFQ-cb). The beam is then released in bunches, reduced in energy through the pulsed-drift tube to 3.2 keV, and captured in a time-of-flight spectrometer (MR-ToF MS) at 2 keV. After about 50 ms, the ions are released, and their flight time to an ion detector is measured. An example ToF spectrum for  $m/q = 106$  showing strontium-fluoride, indium, and tin is depicted in (b).

time-of-flight (ToF) mass spectrometer at TRIUMF, Canada, measured down to  $^{104}\text{Sn}$  [25].

Investigations of local trends of the mass surface surrounding  $^{100}\text{Sn}$  have shown several inconsistencies when extracting masses from  $Q_{\text{EC}}$  value measurements combined with masses of their daughter nuclei [18]. The mass for  $^{100}\text{Sn}$  itself is known only through two inconsistent  $Q_{\text{EC}}$  value measurements [4,12] in combination with the mass of  $^{100}\text{In}$  [18]. Furthermore, the mass of  $^{103}\text{Sn}$ , similarly extracted through a  $Q_{\text{EC}}$  value, was not included in the latest Atomic Mass Evaluation (AME2020 [26]) due to its conflicting impact on the mass surface, and a value derived from systematic trends was recommended instead.

In the present work, we report precision mass measurements of  $^{103-106}\text{Sn}$  performed by multireflection time-of-flight mass spectrometry at CERN-ISOLDE. We compare the results with nuclear *ab initio* [27,28] and density functional theory calculations [29] and suggest several adjustments of neighboring masses based on this comparison and local binding energy trends in the region.

## II. EXPERIMENT AND DATA ANALYSIS

### A. Radioactive tin production at ISOLDE

Neutron-deficient radioactive tin isotopes were produced at CERN-ISOLDE [17] through proton-induced spallation of  $^{139}\text{La}$  nuclei,

$$^{139}\text{La}(p, 8p(19+x)n)^{113-x}\text{Sn}, \quad (1)$$

driven by a 1.4 GeV proton beam delivered by the CERN Proton Synchrotron Booster (PSB) accelerator. Figure 1 shows a

schematic of the apparatus for the production, separation, and mass measurement of the radioactive isotopes.

The target material in the form of lanthanum carbide ( $\text{LaC}_x$ ) with a density of  $5 \text{ g/cm}^2$  (ISOLDE target unit number 774) was bombarded by 1 to 2  $\mu\text{A}$  of protons on average. Each PSB cycle, with a maximum repetition rate of one pulse every 1.2 s, contained  $(1-3) \times 10^{13}$  protons per cycle. Reaction products diffused through and effused out of the porous target material into a small tantalum tube, connecting the target container to the hot-cavity resonance ionization laser ion source (RILIS) [30]. A three-step resonance ionization scheme was used to selectively ionize tin isotopes, shown in panel (a) in the center of Fig. 1.

Different low-lying electronic states in the tin atom were populated as the radioactive isotopes were produced in the target container heated up to  $1900^\circ\text{C}$ . To maximize ionization efficiency, two first excitation steps were used in parallel, starting from the  $5s^2 5p^2 \ ^3P_0$  ground state and the first thermally populated state  $5s^2 5p^2 \ ^3P_1$ . Both transitions led to the  $5s^2 5p6s \ ^3P_1$  state at  $34914.28 \text{ cm}^{-1}$ , and the light used to excite them was generated via frequency tripling a titanium:sapphire (Ti:Sa) laser to produce 286.4 nm and frequency doubling a dye laser to produce 301.0 nm. The thermal populations of the two levels strongly depend on the temperature of the ion source but are almost equal at  $1900^\circ\text{C}$ . During the experiment, an ionization-efficiency enhancement of roughly 70% could be observed when using the transition from the thermally populated state in addition to the excitation of the ground state. A fundamental Ti:Sa laser drove the second step at 811.6 nm, exciting the  $5s^2 5p6s \ ^3P_1^o \rightarrow 5s^2 5p6p \ ^3P_2^o$  transition. An autoionizing transition at 823.7 nm, driven by a Ti:Sa laser, was used as the final step.

The ionized tin isotopes were then extracted from the target and ion source front end and accelerated as a beam of singly charged radioactive ions at 30 keV. Tin ions of interest were separated from the extracted ion beam based on their mass-over-charge ratio  $m/q$  using the high resolution separator (HRS), which consists of two successive electromagnets depicted in dark grey in Fig. 1. The tin ions were finally delivered to the ISOLTRAP mass spectrometer [31], shown at the bottom of Fig. 1.

### B. Mass measurement method

At the mass spectrometer, the ion beam was first decelerated and captured in a linear radio-frequency quadrupole cooler/buncher (RFQ-cb) [32], using helium buffer-gas cooling to improve beam emittance and to create a bunched beam with temporal bunch sizes of the order of several tens of nanoseconds. After a cooling time of 10 ms, the ion bunch was released from the trap and reaccelerated to 30 keV. To capture the ion bunch in the multireflection time-of-flight mass spectrometer (MR-ToF MS) [33], the ion kinetic energy was first reduced from 30 to 3.2 keV using a pulsed drift tube between the RFQ-cb and the MR-ToF MS, and once more from 3.2 to 2 keV using a pulsed drift tube between the two electrostatic mirrors of the mass spectrometer. Trapped inside the device, the ion bunch was reflected between the mirrors for up to 2000 turns before being ejected using the same pulsed drift tube, the so-called in-trap lift [34]. The ion ToF was then measured using a MagneTOF<sup>TM</sup> Mini 14924 electron multiplier detector downstream of the device.

The atomic mass  $m$  of the ions can be extracted using the measured time of flight  $t$  with respect to two reference masses  $m_1$  and  $m_2$  and their ToFs  $t_1$  and  $t_2$  as

$$\sqrt{m} = C_{\text{ToF}} \Delta_{\text{Ref}} + \Sigma_{\text{Ref}}/2, \quad (2)$$

where  $\Delta_{\text{Ref}} = \sqrt{m_1} - \sqrt{m_2}$ ,  $\Sigma_{\text{Ref}} = \sqrt{m_1} + \sqrt{m_2}$ , and  $C_{\text{ToF}} = (2t - t_1 - t_2)/[2(t_1 - t_2)]$  [35]. As reference ions, the isobaric indium isotope from the same spectrum and  $^{87}\text{Rb}^+$  from interleaved reference measurements provided by a surface-ionization source at ISOLTRAP were used. The mass-resolving power of the device is defined as

$$R = \frac{m}{\Delta m} = \frac{t}{2\Delta t_{\text{FWHM}}}, \quad (3)$$

where two different components in the ToF spectrum are considered fully resolved when their separation is at least twice the full width at half maximum (FWHM) of their ToF distribution.

The MR-ToF MS was operated in near-isochronous mode, in which faster ions penetrate the reflecting mirror potential deeper than slower ions, leading to longer turnaround times, thus compensating for their higher velocities. In such a way, the time focus was retained for long storage times, i.e., up to 50 ms, thereby improving resolving power and resolution. This mode of operation was achieved by precisely tuning the ion kinetic energy inside the device by means of the in-trap lift voltage during pulsing. An example ToF spectrum for  $m/q = 106$  is depicted in panel (b) of Fig. 1.

Beam impurities worsen the signal-to-noise ratio and lead to systematic shifts of the ToF due to the electromagnetic interaction with other cotrapped species. This effect is not well understood and is usually mitigated by allowing only a small amount of charges to revolve in the device at any given time. Recent simulations have suggested that systematic ToF shifts may not only worsen with the number of charges in the device but also with the effective separation in the  $m/q$  ratio, which affects species with similar  $m/q$  stronger than less similar species [36]. In-trap deflector electrodes can remove unwanted contaminants that are well separated in time-of-flight from the species of interest through pulsed transversal electric fields [37], which in many cases only applies to non-isobaric contamination or polyatomic molecules. For species requiring higher resolving powers (on the order of  $R < 10^5$ ), mass selective axial ejection through fast switching of either one of the mirror electrodes or the in-trap pulsed drift tube [34], with subsequent retrapping in an RFQ-cb and reinjection into the MR-ToF MS, can suppress isobaric contamination by several orders of magnitude [38].

### C. Target and ion source performance

The yield of  $^{106}\text{Sn}^+$  was tracked to monitor possible target microstructure degradation and the stability of the RILIS, as well as to optimize target and ion source heating for efficiency and beam purity. Figure 2 (left) shows the normalized yield of the extracted  $^{106}\text{Sn}^+$  versus time. Yields on the order of  $10^5$  to  $10^6$  ions/s were observed but dropped on average by one order of magnitude.

Lower ion source temperatures strongly suppressed isobaric contamination, such as indium and strontium monofluoride, which are parasitically surface ionized in the hot environment of the ion source and transfer line, shown in Fig. 2 (right). The highest yields and lowest contamination levels were observed for increased target heating and lower ion source temperatures, facilitating the diffusion and effusion of reaction products through the target material and reducing the degree of parasitic surface ionization.

Besides the decrease in positive ion density, the thermal emission of electrons from the walls of the ion source decreases with lower temperature, while a surplus of negative charges is detrimental for ion confinement [39,40]. Additionally, a lower heating current implies a smaller Ohmic voltage gradient along the ion source, which leads to a slower drift of ions towards the extraction electrode. The increase in yield at lower ion source temperatures in Fig. 2 (right) is most likely due to a slightly lower target temperature [1650(50)°C] as compared to the higher temperatures in the shaded areas of the figure [1730(50)°C].

The target was operated at or above 1700(50)°C to promote quick diffusion and effusion from the target material. A drop in yield over time was observed, which can be attributed to the operation of the target container at temperatures at which  $\text{LaC}_x$  undergoes sintering, decreasing the target material's open porosity [41] and reduces the effusion rate of the radioactive isotopes. Furthermore, the sublimation temperature of pure  $\text{LaC}_2$  in vacuum is near 1700°C, at which the target material starts to volatilize, further worsening the

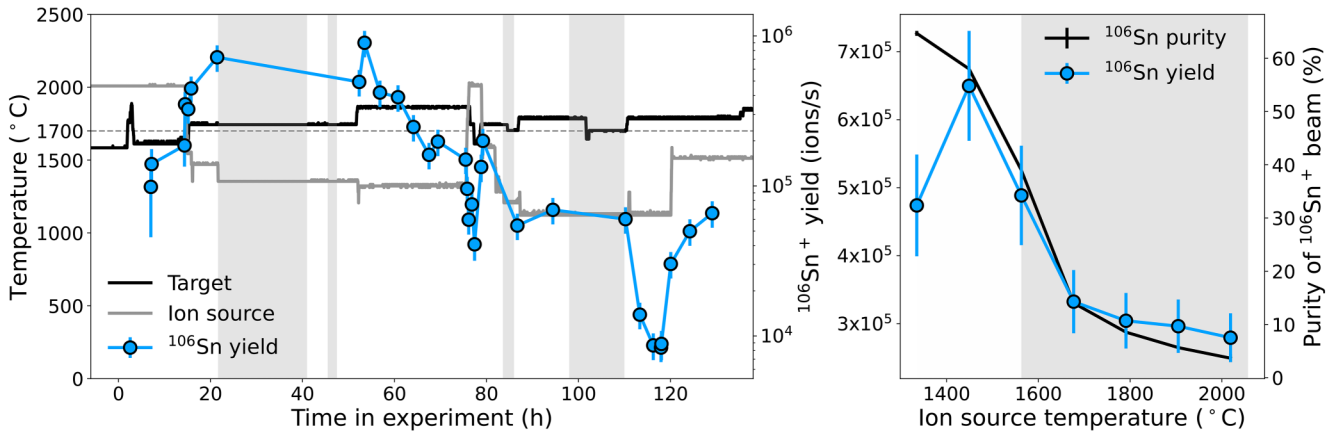


FIG. 2. Left: Normalized yields (in ions per second normalized to  $1 \mu\text{A}$  of protons on target) of the extracted  $^{106}\text{Sn}^+$  beam as measured by ISOLTRAP throughout the experiment with respect to target and ion source temperatures. The temperatures were calibrated using an optical pyrometer for a range of applied heating currents and powers, with measurement uncertainties of about  $50^\circ\text{C}$  (not shown). Shaded areas indicate where protons from the PSB were not available. The grey dashed line indicates the temperature at which the target material starts to undergo sintering. Right: Normalized yield and beam purity (percentage of tin ions in the MR-ToF spectrum) of the extracted  $^{106}\text{Sn}^+$  beam versus ion-source temperature. The target temperature in the shaded area was  $1650(50)^\circ\text{C}$  and in the nonshaded area it was  $1730(50)^\circ\text{C}$ .

target's release properties. Additionally, the energy deposited by the pulsed proton beam leads to mechanical stress and a local hotspot, accelerating the deterioration of the target microstructure.

Figure 3 shows the best yields for observed neutron-deficient tin isotopes. These are compared with previously reported values from the ISOLDE yield database [42,43], to in-target production simulations (available in the same database) [44–46], and to empirical in-target production cross-section calculations [47]. On average, the yields were

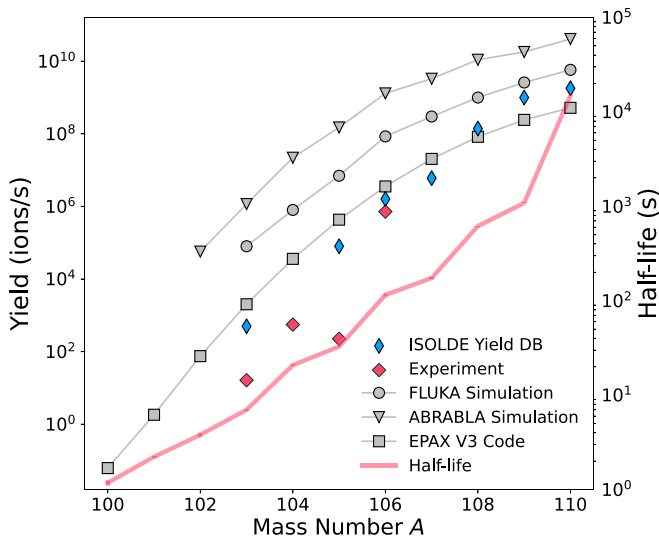


FIG. 3. Best yields extracted from the target measured with the MR-ToF MS (red) and normalized to a proton current of  $1 \mu\text{A}$ . In comparison, previously measured yields of extracted beams reported in the ISOLDE yield database (blue) and in-target production simulation codes FLUKA [44,45] and ABRABLA [46], as well as the empirical fragmentation production cross section code EPAX-V3 [47].

significantly lower than previously reported best yields from the same target and ion source combination at ISOLDE (compare red and blue diamonds) [20,42]. The measured yield for  $^{105}\text{Sn}^+$  is disproportionately lower than the trend would suggest, most likely caused by a low ion source temperature of  $1150(50)^\circ\text{C}$  used during that specific measurement, which was also observed to have a negative impact on the extracted yield of  $^{106}\text{Sn}$  [see Fig. 2 (right)].

The trends and values of the different production simulations for the tin isotopes closer to stability match the measurements within one order of magnitude on average, as most of the produced isotopes in the target can be extracted and ionized due to their long half-lives. For isotopes with half-lives well below  $1 \times 10^4$  s, the trend deviates significantly from the calculated in-target production cross section, indicating large losses during the extraction process due to target-release characteristics, ionization efficiency, and radioactive decay [48].

In recent investigations, yields for other isotopes near  $^{100}\text{Sn}$  have been measured from  $\text{LaC}_x$  target material in combination with RILIS and the ISOLTRAP MR-ToF MS to inform possible future spectroscopy and spectrometry experiments. For cadmium ( $Z = 48$ ) and indium ( $Z = 49$ ), yields on the order of  $10^{-1}$ – $10^0$  ions per second extracted and ionized from the target were found for  $^{97}\text{Cd}$  [49] and  $^{99}\text{In}$  [19]. Antimony ( $Z = 51$ ) was only observed up to  $^{107}\text{Sb}$  with a few  $10^2$  ions per second [50] while more neutron-deficient antimony isotopes were inaccessible at ISOLTRAP due to strong SrF contamination. Based on the data, the extraction rates for the  $N = Z$  isotopes  $^{96}\text{Cd}$ ,  $^{98}\text{In}$ , and  $^{100}\text{Sn}$  from  $\text{LaC}_x$  target material are expected to be on the order of  $10^{-3}$ – $10^{-2}$  ions per second at ISOLDE, which is too low to perform precision experiments.

The future ISOLDE beam dump consolidation and PSB transfer line upgrade will eventually increase proton energies up to 2 GeV at up to  $6 \mu\text{A}$  [51]. While higher energy may not benefit fragmentation yields from  $\text{LaC}_x$ , increased beam

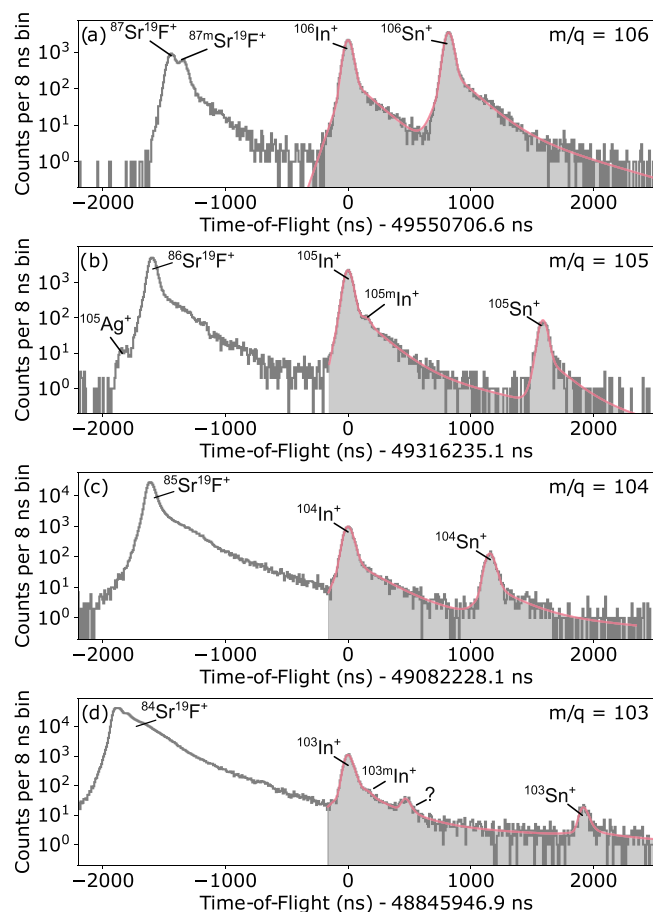


FIG. 4. Typical ToF spectra for the four tin isotopes investigated in the present study. The grey-shaded area indicates the fit range, which excludes the potentially saturated peaks at smaller ToFs. The red line shows the fit to the data. The horizontal axis is centered at the indium peak.

current can result in higher production, even though detrimental effects on target materials from higher proton beam currents need to be systematically investigated. In-flight fragmentation facilities with powerful driver beams and dedicated mass spectrometers, such as LEBIT at FRIB [52] and the ZeroDegree MRToF at RIKEN [53] will very likely benefit from the expected high yields in the  $^{100}\text{Sn}$  region, which are expected to exceed the ISOL method at existing facilities by a few orders of magnitude [54,55].

#### D. ToF spectra and fitting

Figure 4 shows ToF data of the four different mass measurements presented in this study. In all spectra, the surface-ionized strontium-fluoride and indium contaminants are present. While for  $m/q = 106$ , this contamination could be reduced to less than 40% [shown in Fig. 2 (right)], for smaller  $m/q$  values, the contamination gradually increased to >99.9% of the isobaric beam.

To calculate the atomic masses as shown in Eq. (2), the ToF was extracted by fitting a multicomponent exponentially modified Gaussian distribution (“hyper-EMG”) [56] to the

data. Fits with different components were tested to determine the necessary number of components for the fit function, and the resulting reduced chi-squared value  $\chi_{\text{red}}^2$  was observed. One negative component and three positive components resulted in  $\chi_{\text{red}}^2 < 10$ , sufficiently representing the data without leading to parameter overfitting. The final fit was performed using unbinned maximum likelihood estimation, implemented in CERN’s ROOFIT MINUIT minimizer [57]. With 2000 revolutions resulting in storage times of up to 50 ms in the MR-ToF MS, mass resolving powers  $R$  of up to 300 000 were achieved during the experimental campaign, which proved sufficient to resolve the isomeric states in the odd-even indium isotopes and in  $^{87}\text{Sr}$  (with excitation energies of about 650 and 390 keV, respectively).

Due to the intense contamination levels on  $m/q = 104$  and  $m/q = 103$ , only the ToF range between indium and tin was fitted for all masses. This prevented systematic effects resulting from detector and data acquisition saturation around the arrival time of the  $\text{SrF}^+$  ions from being introduced into the shape of the fit function. For the fitted time range, the average count rate was well below five ions per experimental cycle, which prevented detector pileup (the single-ion detector response of the detector is about 1.5 ns long for a MagneTOF<sup>TM</sup> Mini 14924) and loss of signals due to data acquisition dead time (<100 ps for FAST ComTec MCS6A). Furthermore, the ion load in the MR-ToF MS was kept well below 20 ions per cycle to avoid space-charge effects that can lead to systematic ToF shifts [36].

In Fig. 4(a), an example of the spectra for  $m/q = 106$  is shown, where one can see, from left to right, the contamination  $^{87}\text{Sr}^{19}\text{F}^+$  and  $^{106}\text{In}^+$ , as well as the isotope of interest,  $^{106}\text{Sn}^+$ . Interestingly, as noticed during the systematic measurements of this mass-over-charge ratio throughout the experiment, the shoulder on the  $^{87}\text{Sr}^{19}\text{F}^+$  peak only appeared after several tens of hours into the experiment. The observed ToF matches that of a strontium-fluoride molecule containing the long-lived  $I = 1/2$  isomeric state with an excitation energy of 389 keV, leading to a slightly longer ToF. The involved timescales of the isomer’s appearance suggest that the strontium isomer is not directly produced through nuclear reactions but rather through the in-target  $\beta$  decay of the  $I = 1/2$  ground state of  $^{87}\text{Y}$  with a half-life of almost  $T = 80$  h [59]. A typical measurement of the beam composition on this  $m/q$  value took 5 min. Figure 4(a) shows data for about 20 min of measurement time.

Figure 4(b) shows the data taken for  $m/q = 105$ , where  $^{105}\text{Ag}^+$ ,  $^{86}\text{Sr}^{19}\text{F}^+$ ,  $^{105g}\text{In}^+$ , and  $^{105}\text{Sn}^+$  were present in the beam. In this spectrum, the  $I = 1/2$  isomer of  $^{105}\text{In}$  was observed with an abundance of about 1:80 with respect to the  $I = 9/2$  ground state, and the spectrum was fitted with three individual peaks. The data for this spectrum correspond to a measurement time of about 800 s.

For the ion beam with  $m/q = 104$ ,  $^{85}\text{Sr}^{19}\text{F}^+$ ,  $^{104}\text{In}^+$ , and  $^{104}\text{Sn}^+$  were observed, and the spectrum was fitted with only two individual peaks. Interestingly, the  $I = 1/2$  isomeric state in the  $^{85}\text{Sr}$  containing molecule was not observed, despite the predominant  $\beta$  decay of  $^{85}\text{Y}$  into the isomeric state [60]. The data within this plot were taken in about 1 h of measurement.

TABLE I. Mass measurement results in comparison with storage ring measurements from [23], MR-ToF MS measurements from [25], and the AME2020, which is based on the Penning trap measurements reported in [8]. Spin assignments  $J^\pi$ , half-lives, and reference masses ( $^A\text{In}$  for mass  $m_1$ , and  $^{87}\text{Rb}$  for mass  $m_2$ ) are taken from the AME2020. Values marked with # are extrapolated or assigned from systematics.

A	$J^\pi$	Half-life	Ref. $m_1$	$C_{\text{ToF}}$	Mass excess (keV)				
					This work	AME2020 [58]	Lanzhou [23]	LEBIT [24]	TITAN [25]
103	5/2 <sup>+</sup> #	7.0(2)s	$^{103}\text{In}^+$	0.500484342(920)	-67104(18)	-67090(100)#	-67138(68)	-67125.9(37)	
104	0 <sup>+</sup> #	20.8(5)s	$^{104}\text{In}^+$	0.500275256(476)	-71629(10)	-71627(6)			-71601(50)
105	5/2 <sup>+</sup> #	32.7(5) s	$^{105}\text{In}^+$	0.500358319(329)	-73348(13)	-73338(4)			-73349(34)
106	0 <sup>+</sup> #	1.92(8)min	$^{106}\text{In}^+$	0.500175627(71)	-77346(14)	-77354(5)			-77327(37)

On  $m/q = 103$ , one can notice the increase of contamination in the beam: the  $^{84}\text{Sr } ^{19}\text{F}^+$  peak on the left is saturating the discriminator-based data acquisition (note the double-peak structure and the pronounced tailing). Again, both isomer and ground state in  $^{103}\text{In}^+$  were resolved. However, one additional peak appears between the two indium states and  $^{103}\text{Sn}^+$  on the right-hand side of the spectrum, which is inconsistent with any isobaric mass or previously observed surface-ionized molecule. It cannot be ruled out that this species was ejected from the MR-ToF MS on a different revolution number than the other isotopes, hence not having traveled the same distance. Such contamination can usually be investigated by varying the overall trapping time and observing the relative number of peaks in the spectra. This was not attempted due to the limited time available for these  $m/q$  settings. As mentioned in Sec. II C, due to the high operation temperature and proton current during long periods of time, which most likely led to target material sintering, yields for the more short-lived tin isotopes dropped quickly throughout the experiment. As a result, the ratio of  $^{103}\text{Sn}^+$  versus contamination in the beam worsened throughout the experiment, preventing the measurement of the lighter neutron-deficient tin isotopes. Effectively, 2.4 h of data from the first day after the start of the experiment are included in the plot and the analysis of the final mass value.

Due to the beam quality during this experiment, mass selective retrapping [38] as introduced in Sec. II B for contamination suppression is currently being implemented at ISOLTRAP with a second RFQ-cb downstream of the MR-ToF MS.

### III. RESULTS AND DISCUSSION

Table I shows the results for  $^{103-106}\text{Sn}$ , together with available literature values on mass excesses and half-lives, as well as tentative spin assignments. The references for extracting the mass of the ion of interest were consistently taken from the isobaric indium ions and from  $^{87}\text{Rb}^+$  provided by the ISOLTRAP offline ion source. All mass excess values are in very good agreement with the available literature data of the AME2020 [58], the storage ring measurements from Lanzhou [23], and the MR-ToF MS measurements from TITAN at TRIUMF [25]. The experimental uncertainty is between 10 and 20 keV, reaching a precision of about  $\delta m/m \approx 2 \times 10^{-7}$ . The reported mass on  $^{103}\text{Sn}$  is a factor of 4 more precise than the storage ring measurement  $[-67138(68)\text{keV}]$  [23] and, in combination with the other mass measurements, allows

evaluation of the mass surface in the neutron-deficient tin region. With this new measurement, we can deduce the  $Q_{\text{EC}}$  value for the decay of  $^{103}\text{Sn}$  into  $^{103}\text{In}$  to be 7528(20) keV, compared to 7640(70) keV reported in [61], which was extracted from total absorption spectroscopy and  $\beta$ -delayed proton energy measurements.

To investigate the impact of the shift and increased precision of the  $^{103}\text{Sn}$  mass measurement on the local mass surface, the two-neutron separation energy

$$S_{2n}(Z, N) = B(Z, N - 2) - B(Z, N) \quad (4)$$

and the odd-even staggering estimator

$$\Delta_{3n} = 0.5 \times (-1)^N \times [B(Z, N - 1) - 2 \times B(Z, N) + B(Z, N + 1)] \quad (5)$$

are calculated, where  $B(Z, N) = M_E(N, Z) - Z \cdot M_E(^1\text{H}) - N \times M_E(n)$  is the total nuclear binding energy, which consists of the nuclear mass excess  $M_E(N, Z)$  of the nucleus of interest and the mass excesses of the hydrogen atom  $^1\text{H}$  and the mass excess of the neutron. The  $S_{2n}$  filter is regularly used to evaluate shell closures and the sudden change of nuclear deformation. Typically, one analyzes the change of slope in  $S_{2n}$  values with the addition or removal of neutrons, especially at magic numbers. Complementarily, the  $\Delta_{3n}$  filter quantifies the strength of the odd-even staggering along an isotopic chain.

The two mass filters are plotted in Fig. 5, comparing mass values extracted based on  $Q_{\text{EC}}$  values for  $^{101-103}\text{Sn}$  (grey) and direct mass measurements for  $^{103-108}\text{Sn}$  (red) with nuclear *ab initio* calculations from [18] and density functional theory (DFT) calculations described in Ref. [62] and references therein. In the upper panel, using the  $S_{2n}$  filter, one can observe a smooth evolution in the binding energy differences above the expected shell closure at  $N = 50$ . This smooth trend is irregular at  $N = 53$  and at  $N = 55$  when using masses for  $^{101-103}\text{Sn}$  derived using  $Q_{\text{EC}}$  links. This irregularity is further highlighted by plotting the odd-even staggering estimator, shown in the lower panel of Fig. 5.

Extracting masses through  $\beta$  end-point energies requires complete knowledge of the feeding into excited states in the daughter nucleus to reliably fit the  $\beta$ -decay spectrum. High-resolution  $\gamma$  spectroscopy of the decay is needed to account for all internal transitions, and total absorption spectroscopy as well as energy measurements of the delayed proton emission are needed to draw a full picture of the decay. However, incomplete knowledge of the full decay chain caused by internal  $\gamma$  conversion or undetected weak decay branches may

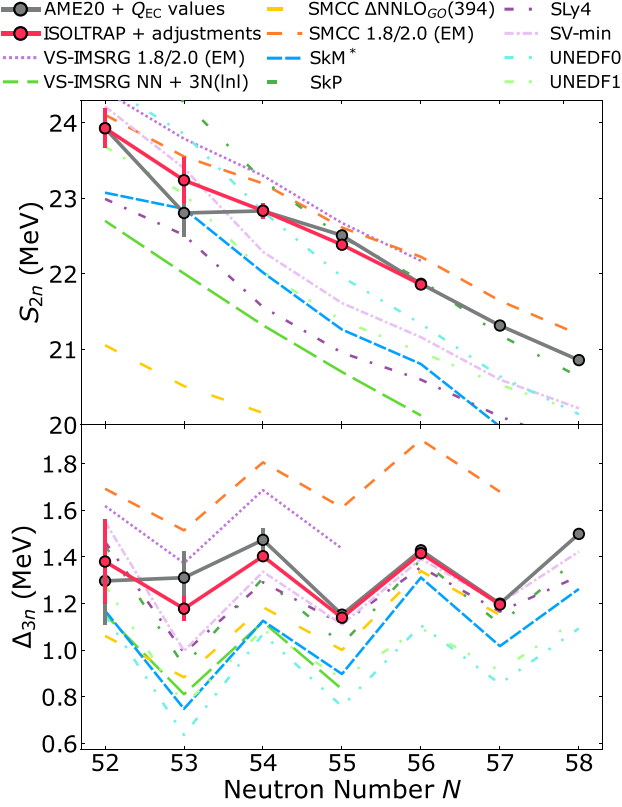


FIG. 5. Evaluated two-neutron separation energy (top) and odd-even staggering estimator (bottom) from masses reported in the AME2020 (grey), the ISOLTRAP measurement with adjustments (red), nuclear *ab initio* calculations from [18], and DFT calculations from [62]. The grey data points include the masses of  $^{101-103}\text{Sn}$  calculated with the  $Q_{EC}$  value measurements from [61,63,64]. The red points include this work’s mass measurement of  $^{103}\text{Sn}$  and the extrapolated mass value for  $^{101}\text{Sn}$ .

lead to significant systematic errors. In the 2020 Atomic Mass Evaluation of input data [26], the mass of  $^{101}\text{Sn}$  is extracted through a  $\beta$ -delayed proton decay channel via  $^{101}\text{In}$  into  $^{100}\text{Cd}$ , with a dominating mass uncertainty of 300 keV assigned from a measurement of the proton emission energy and branching ratios, reported in a scientific report at GSI [63]. Similarly, the ground-state mass of  $^{102}\text{Sn}$  is extracted from the  $^{102}\text{In}$  ground-state mass using the  $Q_{EC}$  value measured in [64], incorporating the 100 keV measurement uncertainty. Additionally,  $^{103}\text{Sn}$  was deemed a “seriously irregular mass” determined only from the  $^{103}\text{In}$  ground-state mass through the  $Q_{EC}$  value measurement from Ref. [61], which led to its rejection from the AME2020 [26]. Finally, the precise mass measurement of  $^{100}\text{In}$  from Ref. [18] highlighted another discrepancy, namely the competition between the results of the two direct  $\beta$ -decay measurements of  $^{100}\text{Sn}$  [4,12], whose  $Q_{EC}$  values disagree on a  $2\sigma$  uncertainty level.

Based on the present precise mass measurements, we reevaluate the mass values expected from systematic trends and from comparing them to theoretical calculations. The present  $^{103}\text{Sn}$  mass excess of  $-67104(18)$  keV makes this

TABLE II. Mass excess values derived from the extrapolated mass of  $^{101}\text{Sn}$  and present measurements of  $^{103}\text{Sn}$  combined with Ref. [23]. The reevaluated mass excess values are compared to those reported in the AME2020 [58]. Values marked with # are extrapolated from the mass surface, and values marked with \* are based on the present adjustment of  $^{101}\text{Sn}$ .

	Mass excess (keV)	AME2020 (keV)
$^{101}\text{Sn}$	$-60005(300)*$	$-60305(300)\#$
$^{103}\text{Sn}$	$-67105(16)$	$-67092(100)\#$
$^{104}\text{Sb}$	$-59307(22)$	$-59340(100)\#$
$^{105}\text{Te}$	$-52510(300)*$	$-52810(300)\#$
$^{107}\text{Te}$	$-60670(17)$	$-60660(100)\#$
$^{108}\text{I}$	$-52784(21)$	$-52770(100)\#$
$^{109}\text{Xe}$	$-45870(300)*$	$-46170(300)\#$
$^{111}\text{Xe}$	$-54530(60)$	$-54520(120)\#$
$^{112}\text{Cs}$	$-46430(60)$	$-46415(120)\#$

nucleus about 130 keV less bound compared to the value of  $-66970(70)$  keV extracted from the  $Q_{EC}$  value. However, to fully remove the kink at  $N = 53$ , one must also adjust the mass of  $^{101}\text{Sn}$ , which contributes in equal parts to the  $S_{2n}$  value. By adding  $+300$  keV to the mass excess of  $^{101}\text{Sn}$ , within two standard deviations of the reported  $\beta$ -delayed proton energy measurement [63], one obtains a smooth trend, as highlighted by the red data point in Fig. 5. We motivate this adjustment not only by comparing the local trends of the mass surface near the shell closure in  $N = 50$  but also based on the predicted trends by the nuclear *ab initio* and DFT calculations. While not all methods, interactions, and functionals predict the correct magnitude of the  $S_{2n}$  value, all calculations predict a flat trend.

In contrast to extracting masses through  $\beta$ -decay endpoint energies, nuclear  $\alpha$  decay is an intrinsically accurate method as the kinetic energies of the emitted  $\alpha$  particles are monoenergetic and relatively easy to measure with keV precision. A unique feature of the nuclear landscape is the small island of  $\alpha$  emitters with decay chains ending in neutron-deficient tin isotopes. Most of the mass data of those short-lived isotopes are indirectly known based on anchoring tin masses through successive  $\alpha$  decays by measuring the  $\alpha$  particles’ energies; see for example Ref. [5,6]. By directly measuring  $^{101-103}\text{Sn}$ , one can significantly reduce the mass uncertainties for antimony, tellurium, iodine, xenon, and cesium isotopes, which are otherwise very challenging for ion-trap-based atomic mass measurements. Table II shows mass excess values, which are based on our  $^{103}\text{Sn}$  mass measurement combined with the measurement of Ref. [23] and the proposed  $^{101}\text{Sn}$  mass adjustment.

The masses from Table II in combination with the mass tables from the AME2020 can be used to plot the  $S_{2n}$  values for a large range of isotopes ( $Z = 41-56$ ), shown in Fig. 6. On a more global picture, the trends for the  $S_{2n}$  values are extremely smooth above the  $N = 50$  shell closure for nuclei below with  $Z < 50$ , where all necessary masses for the evaluation are known to sufficient precision. This smoothness has now been recovered for the tin chain. Above  $Z = 50$ , one notices significant changes at  $N = 55$  in the tellurium chain



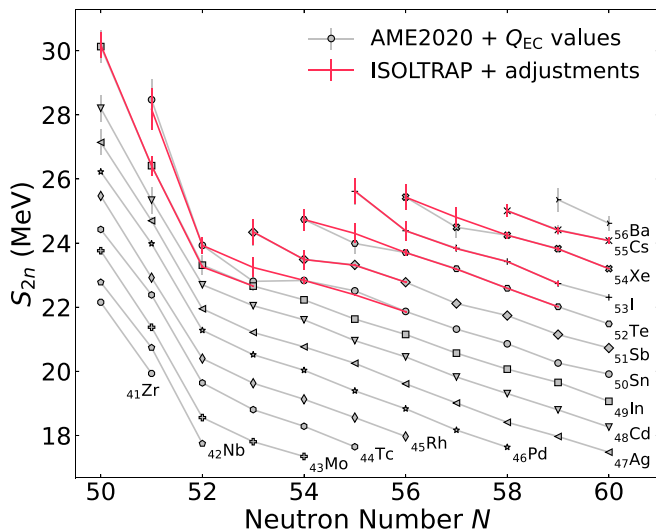


FIG. 6. Evaluated two-neutron separation energy from masses reported in the AME2020 including the masses of  $^{101-103}\text{Sn}$  calculated from  $Q_{\text{EC}}$  value measurements [61,63,64] (grey) or readjusted as shown in Table II following the ISOLTRAP mass measurements from this work (red). Plotted improvements on indium mass uncertainties are taken from [18,19].

and at  $N = 57$  in the xenon chain, leading to overall smoother trends as well.

The smooth decrease in  $S_{2n}$  values for the presented isotopic chains above  $N = 50$  suggests the absence of deformation-dependent variation in binding energies. This is in contrast to what was observed, for example, above  $N = 50$  in a region of nuclear shape transition near  $A = 100$  formed between the neutron-rich krypton ( $Z = 36$ ) and molybdenum ( $Z = 42$ ) isotopic chains [65,66], where the  $S_{2n}$  locally changes its slope from negative to positive, indicating sudden changes in correlation energy.

Lastly, many isotopes presented in Table II are located at the end point of the astrophysical  $rp$  process which is predicted to occur on mass-accreting neutron stars [7]. In the SnSbTe cycle, neutron-deficient tin, antimony, and tellurium isotopes near the proton drip line are produced through proton capture and  $\beta$  decay, where  $^{106-108}\text{Te}$  is unbound against  $\alpha$  decay, recycling tellurium isotopes into tin isotopes. As the proton-separation energy  $S_p$  is negative for  $^{103-105}\text{Sb}$ , the  $(p, \gamma)$  reaction is only possible for  $^{105}\text{Sn}$  and heavier tin isotopes, effectively excluding the lighter antimony and tellurium isotopes from the cycle [8,67]. Our adjustments for the binding energies of  $^{101}\text{Sn}$ ,  $^{104}\text{Sb}$ , and  $^{105}\text{Te}$  are therefore unlikely to affect network calculations for the SnSbTe cycle, while the impact on the improvement of the  $^{103}\text{Sn}$  mass remains to be studied.

#### IV. CONCLUSION

Multireflection ToF mass spectrometry was performed on  $^{103-106}\text{Sn}$  isotopes produced at the radioactive ion beam facility CERN-ISOLDE. Radioactive tin isotopes were produced through nuclear reactions of high-energy protons impinging

on a  $\text{LaC}_x$  target and were ionized through a three-step laser ionization scheme. The target and ion source performance was tracked based on yields of  $^{106}\text{Sn}^+$ , which dropped with time, likely because of sintering of the target material. This study offers a detailed basis for future developments of neutron-deficient tin beams at ISOL facilities and strongly motivates further improvements of ISOL target materials and their degradation over time. The highest yields of extracted  $^{103-106}\text{Sn}^+$  ions were compared to in-target production simulations and empirical cross-section calculations, showing slightly lower values than previously achieved during other experiments at ISOLDE.

All cases suffered from surface-ionized contamination and target degradation, preventing mass measurements of lighter tin isotopes despite sufficient production rates initially estimated from simulations. Atomic masses for  $^{103-106}\text{Sn}$  were obtained, with uncertainties ranging between 10 and 20 keV. The mass uncertainty of  $^{103}\text{Sn}$  was improved by roughly a factor of 4. The measured masses were compared with nuclear *ab initio* and DFT calculations to assess the local smoothness of the mass surface near  $^{100}\text{Sn}$ . It was shown that the extracted masses for  $^{101,103}\text{Sn}$  from  $Q_{\text{EC}}$  value measurements are very likely inaccurate and lead to discrepant trends. Using the more precise mass value of  $^{103}\text{Sn}$  in combination with a mass extrapolation for  $^{101}\text{Sn}$ , this irregularity was removed, recovering smooth trends not only in the tin chain but also in the tellurium and xenon chains.

The mass uncertainty of five other nuclides near the proton drip line, linked to the tin masses through  $\alpha$  decays, was thus improved. This result highlights the necessity for precision mass spectrometry of short-lived radioactive nuclei, since inaccurate  $\beta$ -decay measurements with significant measurement uncertainties—on the order of a few hundreds of keV—can produce misleading trends of the mass filters.

Recently, we were made aware of a publication [24] reporting a Penning-trap mass measurement value for  $^{103}\text{Sn}$  with a measured mass excess of  $-67125.9(37)$  keV. The authors of Ref. [24] draw a similar conclusion considering the smoothness of the mass surface in the tin isotopic chain near  $N = 53$ .

#### ACKNOWLEDGMENTS

The authors gratefully acknowledge technical support from the ISOLDE operations team, the CERN SY-STI-RBS team, and fruitful discussions with U. Köster. They further acknowledge the support of the German Max Planck Society, the French Institut National de Physique Nucléaire et de Physique des Particules (IN2P3), the European Research Council (ERC) under the European Union's Horizon 2020 research and innovation program (Grant Agreements No. 682841 AS-TRUM, No. 654002 ENSAR2, No. 101020842 EUSTRONG, and No. 861198 LISA), as well as the German Federal Ministry of Education and Research (BMBF; Grants No. 05P18HGCI A, No. 05P21HGCI I, and No. 05P21RDFNB). L.N. acknowledges support from the Wolfgang Gentner Programme of the German Federal Ministry of Education and Research (Grant No. 13E18CHA).

The experiment was conducted by M.A.-K., M.Au, D.A., C.B., K.C., P.F., R.H., C.K., D.Lu., D.La., B.M., M.Müller,

M.Mougeot, S.N., L.N., Ch.S., and F.W. Resources and supervision were provided by K.B. and L.S. The manuscript

was prepared by L.N., M.A.-K., K.C., and S.N. All authors contributed to the editing of the manuscript.

- [1] T. Faestermann, M. Górska, and H. Grawe, The structure of  $^{100}\text{Sn}$  and neighbouring nuclei, *Prog. Part. Nucl. Phys.* **69**, 85 (2013).
- [2] M. Lewitowicz, R. Anne, G. Auger, D. Bazin, C. Borcea, V. Borrel, J. Corre, T. Dörfler, A. Fomichov, R. Grzywacz, D. Guillemaud-Mueller, R. Hue, M. Huyse, Z. Janas, H. Keller, S. Lukyanov, A. Mueller, Y. Penionzhkevich, M. Pfützner, F. Pougheon *et al.*, Identification of the doubly-magic nucleus  $^{100}\text{Sn}$  in the reaction  $^{112}\text{Sn} + ^{\text{nat}}\text{Ni}$  at 63 MeV/nucleon, *Phys. Lett. B* **332**, 20 (1994).
- [3] R. Schneider, J. Friese, J. Reinhold, K. Zeitelhack, T. Faestermann, R. Gernhäuser, H. Gilg, F. Heine, J. Homolka, P. Kienle, H. J. Körner, H. Geissel, G. Münzenberg, and K. Sümmerner, Production and identification of  $^{100}\text{Sn}$ , *Z. Phys. A* **348**, 241 (1994).
- [4] C. B. Hinke, M. Böhmer, P. Boutachkov, T. Faestermann, H. Geissel, J. Gerl, R. Gernhäuser, M. Górska, A. Gottardo, H. Grawe, J. L. Grębosz, R. Krücken, N. Kurz, Z. Liu, L. Maier, F. Nowacki, S. Pietri, Z. Podolyák, K. Sieja, K. Steiger *et al.*, Superallowed Gamow–Teller decay of the doubly magic nucleus  $^{100}\text{Sn}$ , *Nature (London)* **486**, 341 (2012).
- [5] K. Auranen, D. Seweryniak, M. Albers, A. D. Ayangeakaa, S. Bottoni, M. P. Carpenter, C. J. Chiara, P. Copp, H. M. David, D. T. Doherty, J. Harker, C. R. Hoffman, R. V. F. Janssens, T. L. Khoo, S. A. Kuvin, T. Lauritsen, G. Lotay, A. M. Rogers, J. Sethi, C. Scholey *et al.*, Superallowed  $\alpha$  decay to doubly magic  $^{100}\text{Sn}$ , *Phys. Rev. Lett.* **121**, 182501 (2018).
- [6] I. G. Darby, R. K. Grzywacz, J. C. Batchelder, C. R. Bingham, L. Cartegni, C. J. Gross, M. Hjorth-Jensen, D. T. Joss, S. N. Liddick, W. Nazarewicz, S. Padgett, R. D. Page, T. Papenbrock, M. M. Rajabali, J. Rotureau, and K. P. Rykaczewski, Orbital dependent nucleonic pairing in the lightest known isotopes of tin, *Phys. Rev. Lett.* **105**, 162502 (2010).
- [7] H. Schatz, A. Aprahamian, V. Barnard, L. Bildsten, A. Cumming, M. Ouellette, T. Rauscher, F.-K. Thielemann, and M. Wiescher, End point of the  $rp$  process on accreting neutron stars, *Phys. Rev. Lett.* **86**, 3471 (2001).
- [8] V.-V. Elomaa, G. K. Vorobjev, A. Kankainen, L. Batist, S. Eliseev, T. Eronen, J. Hakala, A. Jokinen, I. D. Moore, Y. N. Novikov, H. Penttilä, A. Popov, S. Rahaman, J. Rissanen, A. Saastamoinen, H. Schatz, D. M. Seliverstov, C. Weber, and J. Äystö, Quenching of the SnSbTe cycle in the  $rp$  process, *Phys. Rev. Lett.* **102**, 252501 (2009).
- [9] X. Zhou, M. Wang, Y. H. Zhang, Y. A. Litvinov, Z. Meisel, K. Blaum, X. H. Zhou, S. Q. Hou, K. A. Li, H. S. Xu, R. J. Chen, H. Y. Deng, C. Y. Fu, W. W. Ge, J. J. He, W. J. Huang, H. Y. Jiao, H. F. Li, J. G. Li, T. Liao *et al.*, Mass measurements show slowdown of rapid proton capture process at waiting-point nucleus  $^{64}\text{Ge}$ , *Nat. Phys.* **19**, 1091 (2023).
- [10] Z. Wu, L. Guo, Z. Liu, and G. Peng, Production of proton-rich nuclei in the vicinity of  $^{100}\text{Sn}$  via multinucleon transfer reactions, *Phys. Lett. B* **825**, 136886 (2022).
- [11] J. Park, R. Krücken, A. Blazhev, D. Lubos, R. Gernhäuser, M. Lewitowicz, S. Nishimura, D. S. Ahn, H. Baba, B. Blank, P. Boutachkov, F. Browne, I. Čeliković, G. de France, P. Doornenbal, T. Faestermann, Y. Fang, N. Fukuda, J. Giovinazzo, N. Goel *et al.*, Spectroscopy of  $^{99}\text{Cd}$  and  $^{101}\text{In}$  from  $\beta$  decays of  $^{99}\text{In}$  and  $^{101}\text{Sn}$ , *Phys. Rev. C* **102**, 014304 (2020).
- [12] D. Lubos, J. Park, T. Faestermann, R. Gernhäuser, R. Krücken, M. Lewitowicz, S. Nishimura, H. Sakurai, D. S. Ahn, H. Baba, B. Blank, A. Blazhev, P. Boutachkov, F. Browne, I. Čeliković, G. de France, P. Doornenbal, Y. Fang, N. Fukuda, J. Giovinazzo *et al.*, Improved value for the Gamow-Teller strength of the  $^{100}\text{Sn}$  beta decay, *Phys. Rev. Lett.* **122**, 222502 (2019).
- [13] C. Hornung, D. Amanbayev, I. Dedes, G. Kripko-Koncz, I. Miskun, N. Shimizu, S. Ayet San Andrés, J. Bergmann, T. Dickel, J. Dudek, J. Ebert, H. Geissel, M. Górska, H. Grawe, F. Greiner, E. Haettner, T. Otsuka, W. R. Plaß, S. Purushothaman, A.-K. Rink *et al.*, Isomer studies in the vicinity of the doubly-magic nucleus  $^{100}\text{Sn}$ : Observation of a new low-lying isomeric state in  $^{97}\text{Ag}$ , *Phys. Lett. B* **802**, 135200 (2020).
- [14] A. Mollaebrabimi, C. Hornung, T. Dickel, D. Amanbayev, G. Kripko-Koncz, W. R. Plaß, S. Ayet San Andrés, S. Beck, A. Blazhev, J. Bergmann, H. Geissel, M. Górska, H. Grawe, F. Greiner, E. Haettner, N. Kalantar-Nayestanaki, I. Miskun, F. Nowacki, C. Scheidenberger, S. Bagchi *et al.*, Studying Gamow-Teller transitions and the assignment of isomeric and ground states at  $N = 50$ , *Phys. Lett. B* **839**, 137833 (2023).
- [15] A. Kankainen, V.-V. Elomaa, L. Batist, S. Eliseev, T. Eronen, U. Hager, J. Hakala, A. Jokinen, I. D. Moore, Y. N. Novikov, H. Penttilä, A. Popov, S. Rahaman, S. Rinta-Antila, J. Rissanen, A. Saastamoinen, D. M. Seliverstov, T. Sonoda, G. Vorobjev, C. Weber *et al.*, Mass measurements and implications for the energy of the high-spin isomer in  $^{94}\text{Ag}$ , *Phys. Rev. Lett.* **101**, 142503 (2008).
- [16] Z. Ge, M. Reponen, T. Eronen, B. Hu, M. Kortelainen, A. Kankainen, I. Moore, D. Nesterenko, C. Yuan, O. Beliuskina, L. Cañete, R. de Groot, C. Delafosse, T. Dickel, A. de Roubin, S. Geldhof, W. Gins, J. D. Holt, M. Hukkanen, A. Jaries *et al.*, High-precision mass measurements of neutron deficient silver isotopes probe the robustness of the  $N = 50$  shell closure, *Phys. Rev. Lett.* **133**, 132503 (2024).
- [17] R. Catherall, W. Andreatza, M. Breitenfeldt, A. Dorsival, G. J. Focker, T. P. Gharsa, G. T. J. J.-L. Grenard, F. Locci, P. Martins, S. Marzari, J. Schipper, A. Shornikov, and T. Stora, The ISOLDE facility, *J. Phys. G: Nucl. Part. Phys.* **44**, 094002 (2017).
- [18] M. Mougeot, D. Atanasov, J. Kartheim, R. N. Wolf, P. Ascher, K. Blaum, K. Chrysalidis, G. Hagen, J. D. Holt, W. J. Huang, G. R. Jansen, I. Kulikov, Y. A. Litvinov, D. Lunney, V. Manea, T. Miyagi, T. Papenbrock, L. Schweikhard, A. Schwenk, T. Steinsberger *et al.*, Mass measurements of  $^{99-101}\text{In}$  challenge *ab initio* nuclear theory of the nuclide  $^{100}\text{Sn}$ , *Nat. Phys.* **17**, 1099 (2021).
- [19] L. Nies, D. Atanasov, M. Athanasakis-Kaklamanakis, M. Au, K. Blaum, J. Dobaczewski, B. S. Hu, J. D. Holt, J. Kartheim, I. Kulikov, Y. A. Litvinov, D. Lunney, V. Manea, T. Miyagi, M. Mougeot, L. Schweikhard, A. Schwenk, K. Sieja, and F. Wienholtz, Isomeric excitation energy for  $^{99}\text{In}^m$  from mass spectrometry reveals constant trend next to doubly magic  $^{100}\text{Sn}$ , *Phys. Rev. Lett.* **131**, 022502 (2023).

- [20] CRIS Collaboration (private communication).
- [21] A. Ekström, J. Cederkäll, C. Fahlander, M. Hjorth-Jensen, F. Ames, P. A. Butler, T. Davinson, J. Eberth, F. Fincke, A. Görgen, M. Górski, D. Habs, A. M. Hurst, M. Huyse, O. Ivanov, J. Iwanicki, O. Kester, U. Köster, B. A. Marsh, J. Mierzejewski *et al.*,  $0_{gs}^+ \rightarrow 2_1^+$  transition strengths in  $^{106}\text{Sn}$  and  $^{108}\text{Sn}$ , *Phys. Rev. Lett.* **101**, 012502 (2008).
- [22] A. Martin, D. Ackermann, G. Audi, K. Blaum, M. Block, A. Chaudhuri, Z. Di, S. Eliseev, R. Ferrer, D. Habs, F. Herfurth, F. P. Heßberger, S. Hofmann, H.-J. Kluge, M. Mazzocco, M. Mukherjee, J. B. Neumayr, Y. Novikov, W. Plaß, S. Rahaman *et al.*, Mass measurements of neutron-deficient radionuclides near the end-point of the rp-process with SHIPTRAP, *Eur. Phys. J. A* **34**, 341 (2007).
- [23] Y. M. Xing, C. X. Yuan, M. Wang, Y. H. Zhang, X. H. Zhou, Y. A. Litvinov, K. Blaum, H. S. Xu, T. Bao, R. J. Chen, C. Y. Fu, B. S. Gao, W. W. Ge, J. J. He, W. J. Huang, T. Liao, J. G. Li, H. F. Li, S. Litvinov, S. Naimi *et al.*, Isochronous mass measurements of neutron-deficient nuclei from  $^{112}\text{Sn}$  projectile fragmentation, *Phys. Rev. C* **107**, 014304 (2023).
- [24] C. M. Ireland, F. M. Maier, G. Bollen, S. E. Campbell, X. Chen, H. Erington, N. D. Gamage, M. J. Gutiérrez, C. Izzo, E. Leistenschneider, E. M. Lykiardopoulou, R. Orford, W. S. Porter, D. Puentes, M. Redshaw, R. Ringle, S. Rogers, S. Schwarz, L. Stackable, C. S. Sumithrarachchi *et al.*, preceding paper, High-precision mass measurement of  $^{105}\text{Sn}$  restores smoothness of the mass surface, *Phys. Rev. C* **111**, 014314 (2025).
- [25] A. Czihaly, S. Beck, J. Bergmann, C. L. Brown, T. Brunner, T. Dickel, J. Dilling, E. Dunling, J. Flowerdew, Z. Hockenbery, A. Jacobs, B. Kootte, S. Malbrunot-Ettenauer, F. M. Millán, A. Mollaebrahimi, E. Leistenschneider, E. M. Lykiardopoulou, I. Mukul, S. F. Paul, W. R. Plaß *et al.*, Exploring the western shoreline of the nuclear chart: What precision mass spectrometry with TITAN-TRIUMF can teach us about nuclear existence, *Preprints.org*, <https://doi.org/10.20944/preprints202409.0472.v1>.
- [26] W. Huang, M. Wang, F. Kondev, G. Audi, and S. Naimi, The AME 2020 atomic mass evaluation (I). Evaluation of input data, and adjustment procedures, *Chin. Phys. C* **45**, 030002 (2021).
- [27] S. R. Stroberg, A. Calci, H. Hergert, J. D. Holt, S. K. Bogner, R. Roth, and A. Schwenk, A nucleus-dependent valence-space approach to nuclear structure, *Phys. Rev. Lett.* **118**, 032502 (2017).
- [28] S. R. Stroberg, H. Hergert, S. K. Bogner, and J. D. Holt, Nonempirical interactions for the nuclear shell model: An update, *Annu. Rev. Nucl. Part. Sci.* **69**, 307 (2019).
- [29] *Energy Density Functional Methods for Atomic Nuclei*, edited by N. Schunck (IOP, Bristol, 2019), pp. 2053–2563.
- [30] V. Fedosseev, K. Chrysalidis, T. D. Goodacre, B. Marsh, S. Rothe, C. Seiffert, and K. Wendt, Ion beam production and study of radioactive isotopes with the laser ion source at ISOLDE, *J. Phys. G: Nucl. Part. Phys.* **44**, 084006 (2017).
- [31] M. Mukherjee, D. Beck, K. Blaum, G. Bollen, J. Dilling, S. George, F. Herfurth, A. Herlert, A. Kellerbauer, H.-J. Kluge, S. Schwarz, L. Schweikhard, and C. Yazidjian, ISOLTRAP: An on-line Penning trap for mass spectrometry on short-lived nuclides, *Eur. Phys. J. A* **35**, 1 (2008).
- [32] F. Herfurth, J. Dilling, A. Kellerbauer, G. Bollen, S. Henry, H.-J. Kluge, E. Lamour, D. Lunney, R. Moore, C. Scheidenberger, S. Schwarz, G. Sikler, and J. Szerypo, A linear radiofrequency ion trap for accumulation, bunching, and emittance improvement of radioactive ion beams, *Nucl. Instrum. Methods Phys. Res., Sect. A* **469**, 254 (2001).
- [33] R. Wolf, F. Wienholtz, D. Atanasov, D. Beck, K. Blaum, C. Borgmann, F. Herfurth, M. Kowalska, S. Kreim, Y. A. Litvinov, D. Lunney, V. Manea, D. Neidherr, M. Rosenbusch, L. Schweikhard, J. Stanja, and K. Zuber, ISOLTRAP's multi-reflection time-of-flight mass separator/spectrometer, *Int. J. Mass Spectrom.* **349-350**, 123 (2013).
- [34] F. Wienholtz, S. Kreim, M. Rosenbusch, L. Schweikhard, and R. Wolf, Mass-selective ion ejection from multi-reflection time-of-flight devices via a pulsed in-trap lift, *Int. J. Mass Spectrom.* **421**, 285 (2017).
- [35] F. Wienholtz, D. Beck, K. Blaum, C. Borgmann, M. Breitenfeldt, R. B. Kacirli, S. George, F. Herfurth, J. D. Holt, M. Kowalska, S. Kreim, D. Lunney, V. Manea, J. Menéndez, D. Neidherr, M. Rosenbusch, L. Schweikhard, A. Schwenk, J. Simonis, J. Stanja *et al.*, Masses of exotic calcium isotopes pin down nuclear forces, *Nature (London)* **498**, 346 (2013).
- [36] F. Maier, F. Buchinger, L. Croquette, P. Fischer, H. Heylen, F. Hummer, C. Kanitz, A. Kwiatkowski, V. Lagaki, S. Lechner, E. Leistenschneider, G. Neyens, P. Plattner, A. Roitman, M. Rosenbusch, L. Schweikhard, S. Sels, M. Vilen, F. Wienholtz, and S. Malbrunot-Ettenauer, Increased beam energy as a pathway towards a highly selective and high-flux MR-ToF mass separator, *Nucl. Instrum. Methods Phys. Res. Sect. A* **1056**, 168545 (2023).
- [37] P. Fischer, S. Knauer, G. Marx, and L. Schweikhard, In-depth study of in-trap high-resolution mass separation by transversal ion ejection from a multi-reflection time-of-flight device, *Rev. Sci. Instrum.* **89**, 015114 (2018).
- [38] M. Reiter, S. A. S. Andrés, J. Bergmann, T. Dickel, J. Dilling, A. Jacobs, A. Kwiatkowski, W. Plaß, C. Scheidenberger, D. Short, C. Will, C. Babcock, E. Dunling, A. Finlay, C. Hornung, C. Jesch, R. Klawitter, B. Kootte, D. Lascar, E. Leistenschneider *et al.*, Commissioning and performance of TITAN's multiple-reflection time-of-flight mass-spectrometer and isobar separator, *Nucl. Instrum. Methods Phys. Res. Sect. A* **1018**, 165823 (2021).
- [39] R. Kirchner, Progress in ion source development for on-line separators, *Nucl. Instrum. Methods Phys. Res.* **186**, 275 (1981).
- [40] M. Turek, A. Drożdżel, K. Pyszniak, D. Mączka, and B. Słowiński, Simulations of ionization in a hot cavity surface ion source, *Rev. Sci. Instrum.* **83**, 023303 (2012).
- [41] L. Biasetto, P. Zanonato, S. Carturan, P. Di Bernardo, P. Colombo, A. Andrighetto, and G. Prete, Lanthanum carbide-based porous materials from carburization of lanthanum oxide and lanthanum oxalate mixtures, *J. Nucl. Mater.* **378**, 180 (2008).
- [42] ISOLDE yield database, accessed online in August 2024, <https://isoyields2.web.cern.ch/>.
- [43] J. Ballof, J. Ramos, A. Molander, K. Johnston, S. Rothe, T. Stora, and C. Düllmann, The upgraded ISOLDE yield database – A new tool to predict beam intensities, *Nucl. Instrum. Methods Phys. Res. Sect. B* **463**, 211 (2020).
- [44] T.T. Böhlen, F. Cerutti, M. Chin, A. Fassò, A. Ferrari, P. Ortega, A. Mairani, P. Sala, G. Smirnov, and V. Vlachoudis, The FLUKA code: Developments and challenges for high energy and medical applications, *Nucl. Data Sheets* **120**, 211 (2014).

- [45] C. Ahcida, D. Bozzato, D. Calzolari, F. Cerutti, N. Charitonidis, A. Cimmino, A. Coronetti, G. L. D'Alessandro, A. Donadon Servelle, L. S. Esposito, R. Froeschl, R. García Alía, A. Gerbershagen, S. Gilardoni, D. Horváth, G. Hugo, A. Infantino, V. Kouskoura, A. Lechner *et al.*, New capabilities of the FLUKA multi-purpose code, *Front. Phys.* **9**, 788253 (2022).
- [46] A. Kelic, M. V. Ricciardi, and K.-H. Schmidt, ABLA07—Towards a complete description of the decay channels of a nuclear system from spontaneous fission to multifragmentation, [arXiv:0906.4193](https://arxiv.org/abs/0906.4193).
- [47] K. Sümmerer, Improved empirical parametrization of fragmentation cross sections, *Phys. Rev. C* **86**, 014601 (2012).
- [48] U. Köster, How to produce intense and pure ISOL beams, *Prog. Part. Nucl. Phys.* **46**, 411 (2001).
- [49] M. Mougeot, *Mass Measurement of the Neutron-Deficient  $^{96}\text{Cd}$  with ISOLTRAP*, Technical Report (CERN, Geneva, 2023).
- [50] K. M. Lynch, *Collinear Resonance Ionization Spectroscopy of Neutron-Deficient Antimony Isotopes, Towards the Proton Drip Line*, Technical Report (CERN, Geneva, 2023).
- [51] M. Fraser *et al.*, Upgrade of the PS booster-to-ISOLDE beam transfer line to facilitate an increase in proton driver energy, in *IPAC'24 - Proceedings of the 15th International Particle Accelerator Conference* (JACoW, Geneva, 2024), pp. 3552–3555.
- [52] R. Ringle, S. Schwarz, and G. Bollen, Penning trap mass spectrometry of rare isotopes produced via projectile fragmentation at the LEBIT facility, *Int. J. Mass Spectrom.* **349-350**, 87 (2013).
- [53] M. Rosenbusch, M. Wada, S. Chen, A. Takamine, S. Imura, D. Hou, W. Xian, S. Yan, P. Schury, Y. Hirayama, Y. Ito, H. Ishiyama, S. Kimura, T. Kojima, J. Lee, J. Liu, S. Michimasa, H. Miyatake, J. Moon, M. Mukai *et al.*, The new MRTOF mass spectrograph following the ZeroDegree spectrometer at RIKEN's RIBF facility, *Nucl. Instrum. Methods Phys. Res. Sect. A* **1047**, 167824 (2023).
- [54] H. Okuno, N. Fukunishi, and O. Kamigaito, Progress of RIBF accelerators, *Prog. Theor. Exp. Phys.* **2012**, 3C002 (2012).
- [55] J. Wei, H. Ao, B. Arend, S. Beher, G. Bollen, N. Bultman, F. Casagrande, W. Chang, Y. Choi, S. Cogan, C. Compton, M. Cortesi, J. Curtin, K. Davidson, X. Du, K. Elliott, B. Ewert, A. Facco, A. Fila, K. Fukushima *et al.*, Accelerator commissioning and rare isotope identification at the facility for rare isotope beams, *Mod. Phys. Lett. A* **37**, 2230006 (2022).
- [56] S. Purushothaman, S. Ayet San Andrés, J. Bergmann, T. Dickel, J. Ebert, H. Geissel, C. Hornung, W. Plaß, C. Rappold, C. Scheidenberger, Y. Tanaka, and M. Yavor, Hyper-EMG: A new probability distribution function composed of exponentially modified Gaussian distributions to analyze asymmetric peak shapes in high-resolution time-of-flight mass spectrometry, *Int. J. Mass Spectrom.* **421**, 245 (2017).
- [57] F. James, MINUIT: Function minimization and error analysis reference manual, CERN Program Library Long Writeups (CERN, Geneva, 1998), <https://cds.cern.ch/record/2296388?ln=en>.
- [58] M. Wang, W. Huang, F. Kondev, G. Audi, and S. Naimi, The AME 2020 atomic mass evaluation (II). Tables, graphs and references, *Chin. Phys. C* **45**, 030003 (2021).
- [59] T. D. Johnson and W. D. Kulpa, Evaluated nuclear structure data file, *Nucl. Data Sheets* **129**, 1 (2015).
- [60] B. Singh and J. Chen, Evaluated nuclear structure data file, *Nucl. Data Sheets* **116**, 1 (2014).
- [61] O. Kavatsyuk, M. Kavatsyuk, L. Batist, A. Banu, F. Becker, A. Blazhev, W. Brühle, J. Döring, T. Faestermann, M. Górska, H. Grawe, Z. Janas, A. Jungclaus, M. Karny, R. Kirchner, M. La Commara, S. Mandal, C. Mazzocchi, I. Mukha, S. Muralithar *et al.*, Beta decay of  $^{103}\text{Sn}$ , *Eur. Phys. J. A* **25**, 211 (2005).
- [62] J. Erler, N. Birge, M. Kortelainen, W. Nazarewicz, E. Olsen, A. M. Perhac, and M. Stoitsov, The limits of the nuclear landscape, *Nature (London)* **486**, 509 (2012).
- [63] K. Straub, *GSI Scientific Report 2010* (GSI, Darmstadt, 2010), pp. 151–151.
- [64] T. Faestermann, R. Schneider, A. Stolz, K. Sümmerer, E. Wefers, J. Friese, H. Geissel, M. Hellström, P. Kienle, H.-J. Körner, M. Mineva, M. Münch, G. Münzenberg, C. Schlegel, K. Schmidt, P. Thirolf, H. Weick, and K. Zeitelhack, Decay studies of  $N \approx Z$  nuclei from  $^{75}\text{Sr}$  to  $^{102}\text{Sn}$ , *Eur. Phys. J. A* **15**, 185 (2002).
- [65] S. Naimi, G. Audi, D. Beck, K. Blaum, C. Böhm, C. Borgmann, M. Breitenfeldt, S. George, F. Herfurth, A. Herlert, M. Kowalska, S. Kreim, D. Lunney, D. Neidherr, M. Rosenbusch, S. Schwarz, L. Schweikhard, and K. Zuber, Critical-point boundary for the nuclear quantum phase transition near  $A = 100$  from mass measurements of  $^{96,97}\text{Kr}$ , *Phys. Rev. Lett.* **105**, 032502 (2010).
- [66] V. Manea, D. Atanasov, D. Beck, K. Blaum, C. Borgmann, R. B. Cakirli, T. Eronen, S. George, F. Herfurth, A. Herlert, M. Kowalska, S. Kreim, Y. A. Litvinov, D. Lunney, D. Neidherr, M. Rosenbusch, L. Schweikhard, F. Wienholtz, R. N. Wolf, and K. Zuber, Collective degrees of freedom of neutron-rich  $A \approx 100$  nuclei and the first mass measurement of the short-lived nuclide  $^{100}\text{Rb}$ , *Phys. Rev. C* **88**, 054322 (2013).
- [67] J. Clark, G. Savard, M. Mumpower, and A. Kankainen, Precise mass measurements of radioactive nuclides for astrophysics, *Eur. Phys. J. A* **59**, 204 (2023).